# Sound propagation in isotropically and uni-axially compressed cohesive, frictional granular solids

O. Mouraille [a,b] O. Herbst [a,c] S. Luding [a,b]

[a] *Multi Scale Mechanics, TS, CTW, UTwente,*
*P.O. Box 217, 7500 AE Enschede, The Netherlands*
*e-mail:* s.luding@utwente.nl *e-mail:* o.j.p.mouraille@utwente.nl

[b] *Particle Technology, Nanostructured Materials,*
*DelftChemTech, TNW, TUDelft,*
*Julianalaan 136, 2628 BL Delft, The Netherlands*

[c] *Aerospace Engineering, TU Delft,*
*Kluyverweg 1, 2629 HS Delft, The Netherlands,*
*e-mail:* olaf.herbst@gmx.net

**Abstract**

Using an advanced contact model in DEM simulations, involving elasto-plasticity, adhesion, and friction, pressure-sintered tablets are formed and prepared for unconfined tests. Sound propagation in such packings is studied under various friction and adhesion conditions. Small differences can be explained by differences in the structure that are due to the sensitivity of the packing on the contact properties during preparation history. In some cases the signals show unexpected propagation behavior, but the power-spectra are similar for all values of adhesion and friction tested. Furthermore, one of these tablets is uni-axially and unconfined compressed and the sound propagation characteristics are examined at different strains, (i) in the elastic regime, (ii) during failure, and (iii) during critical flow. Similarly, the results do vary astonishingly little for packings at different externally applied strains.

*Key words:* granular materials, particle simulation contact force-laws, friction, adhesion, elasto-plastic deformation, sound propagation.
*PACS:* 45.70, 47.50+d

## 1 Introduction

Granular Materials in general [1–12] and especially cohesive, frictional, fine powders show a peculiar flow behavior [13–17]. Adhesionless powder flows freely, but when adhesion due to van der Waals forces is strong enough, agglomerates or clumps form, and can break into pieces again [18–21]. This is enhanced by pressure- or temperature-sintering [22] and, under extremely strong pressure, tablets or granulates can be formed [23–26] from primary particles. Applications can be found, e.g. in the pharmaceutical industry.

The basic question is how to understand such cohesive, frictional, fine powders and whether one can use sound propagation measurements from simulations to gain additional insight.

In contrast to crystalline materials [27,28], information propagation in disordered and inhomogeneous granular media is far from well understood, especially when friction and other realistic contact mechanisms are taken into account [29–31]. Understanding better the sound propagation in granular media will improve the interpretation of ultrasound measurements in soil as a non-intrusive way to detect and measure underground structures. This has applications in archeology, seismology and – because of its cost efficiency – for the discovery and exploitation of natural resources such as ores, coal, or oil

Stress-wave or sound propagation through dense granular matter is the superposition of many complex phenomena, which are caused by the discrete, inhomogeneous, anisotropic and dissipative structure of this class of materials. The properties of such waves are strongly affected by phenomena like attenuation, scattering, and dispersion [32]. Ballistic pulse propagation co-exists with slower, multiply scattered coda-like signals [32,33]. The stress- and frequency-dependence of the wave propagation features are subject of ongoing discussion [34,32] in static and shaken packings as well.

Many-particle simulations methods like discrete element models (DEM) [35,36,5,37–40] complement experiments on the scale of small "representative volume elements" (RVEs) [39]. Deep and detailed insight into the kinematics and dynamics of the samples can be obtained since the information about all particles and contacts is available at all times. Discrete Element Models require the contact forces and torques as the basic input, to solve the equations of motion for all particles in a granular system. From this, the macroscopic material properties as, among others, elastic moduli, cohesion, friction, yield strength, dilatancy, or anisotropy can be measured from such RVE tests.

The macroscopic properties are controlled by the "microscopic" contact forces and torques [41,42,32,34,43]. Non-linear contacts [44,40], frequency-dependence [45,46] and also scattering and attenuation in other "particle type" materials

[47] have been reported.

Research challenges involve not only realistic DEM simulations of many-particle systems and their experimental validation, but also the transition from the microscopic contact properties to the macroscopic flow behavior [39,48,15,16,49]. This so-called micro-macro transition [15,16] should allow to better understand the collective flow behavior of many particle systems as a function of the particles' material and contact properties. A continuum description ("macroscopic") of (dense) granular materials can be highly useful for field applications (like oil discovery), since particle simulations ("microscoipc") are not applicable due to the huge system sizes. Some empirical descriptions are available also for dynamic and possibly non-linear deformation and propagation modes [34,32,50].

The paper is organized as follows. After introducing the simulation method in section 2, the preparation of our samples is discussed in section 3. Sound propagation through densely packed granular systems and its dependence on friction and adhesion is examined in section 4.1, while sound propagation for different states of compression and failure is reported in section 4.2. Summary and Conclusions are given in section 5.

## 2 Discrete Particle Model

To simulate packing, failure and sound propagation in a granular material we use a Discrete Element Model (DEM) [35,36,5,37,38,51,25]. Such simulations can complement experiments on small scale by providing deep and detailed insight into the kinematics and dynamics of the samples examined. In the following we briefly introduce the method that allows us to simulate wave propagation in (damaged) packings. The numerics and algorithms are described in text-books [52–54], so that we only discuss the basic input into DEM, i.e., the contact force models and parameters. More details on the the contact model can be found in Ref. [25] and references therein.

The pairwise inter-particle forces typically used are based on the overlap and the relative motion of particles. This might not be sufficient to account for the inhomogeneous stress distribution inside the particles and possible multi-contact effects. However, this simplifying assumption enables us to study larger samples of particles with a minimal complexity of the contact properties, taking into account phenomena like non-linear contact elasticity, plastic deformation, and adhesion as well as friction, rolling resistance, and torsion resistance. In the following we will neglect rolling and torsion resistance however.

Realistic modeling of the deformations of two particles in contact with each other is already quite challenging. The description of many-body systems where each particle can have multiple contacts is extremely complex. We therefore assume our particles to be non-deformable perfect spheres. They shall interact only when in contact. We call two particles in contact when the distance of their centers of mass is less than the sum of their radii. For two spherical particles $i$ and $j$ in contact, with radii $a_i$ and $a_j$, respectively, we define their overlap

$$\delta = (a_i + a_j) - (\boldsymbol{r}_i - \boldsymbol{r}_j) \cdot \boldsymbol{n} > 0 \tag{1}$$

with the unit vector $\boldsymbol{n} := \boldsymbol{n}_{ij} := (\boldsymbol{r}_i - \boldsymbol{r}_j)/|\boldsymbol{r}_i - \boldsymbol{r}_j|$ pointing from $j$ to $i$. $\boldsymbol{r}_i$ and $\boldsymbol{r}_j$ denote the position of paricle $i$ and $j$, respectively.

The force on particle $i$, labelled $\boldsymbol{f}_i$, is modelled to depend pairwise on all particles $j$ with which particle $i$ is in contact, $\boldsymbol{f}_i = \sum_j \boldsymbol{f}^c_{i|j}$, where $\boldsymbol{f}^c_{i|j}$ is the force on particle $i$ exerted by particle $j$ at contact $c$. The force $\boldsymbol{f}^c_{i|j}$ can be decomposed into a normal and a tangential part, $\boldsymbol{f}^c_{i|j} = f^n_{i|j}\boldsymbol{n} + f^t_{i|j}\boldsymbol{t}$, where $\boldsymbol{n} \cdot \boldsymbol{t} = 0$.

To model the force $\boldsymbol{f}^c_{i|j}$ we use an adhesive, elasto-plastic, history-dependent contact law that depends on three variables only and is described in more detail in Ref. [25]: The force between two spheres is modelled to depend only on their overlap $\delta$, the relative velocity of their surfaces, and the maximum overlap $\delta_{\max}$ this contact has suffered in the past. We will leave out the index $i|j$ from now on.

For the normal force $f^n$ we apply a modified spring-dashpot model: The dashpot part is, as usual, a viscous damping force that depends on the normal component of the relative velocity. The spring "constant" $k$, however, is only temporarilly constant and depends on the history of the contact, changing the force from linear in the overlap to piecewise linear: The repulsive force during initial loading is governed by the initial loading stiffness constant $k_1$, see Fig. 1. When the contact is unloaded the maximal overlap $\delta_{\max}$ is kept in memory as a history variable. The forces during un- and reloading can be either repulsive or attractive and are determined using a linear interpolation $k_*$ between the initial loading stiffness constant $k_1$ and the maximal elastic stiffness constant $k_2$. For overlaps greater than $\delta_{\text{material}}$ the stiffness constant $k_2$ is used. When re-loading starts after unloading $\delta_{\max}$ is reset to the then current value of $\delta$ and it is subsequentally increased again during loading. If a contact breaks $\delta_{\max}$ is set to zero. Each contact can be unloaded into the attractive regime with the current stiffness $k_*$. This models adhesion. The attractive forces are

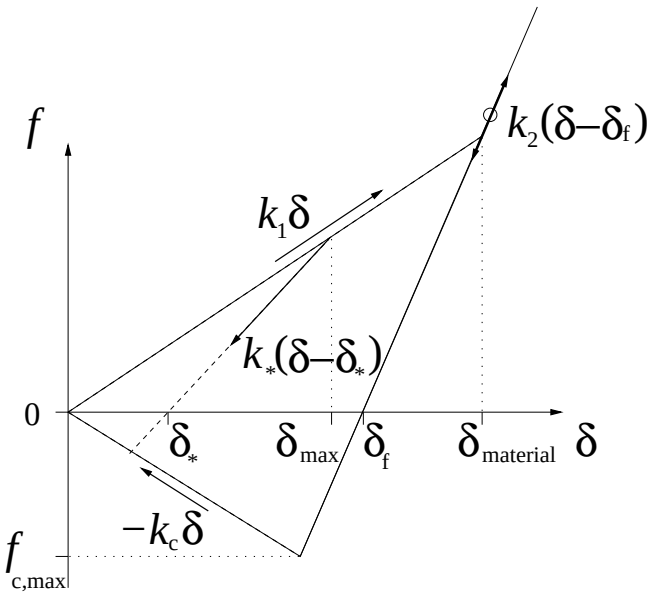


Fig. 1. Spring part of the normal component of the contact force $f^n$, i.e. the part that is a function of the overlap $\delta$. (The viscous normal forces are not included in this plot.) $k_1$, $k_2$, $k_c$, and $\delta_{\text{material}}$ are material constants. $\delta_{\max}$ is the maximum overlap this contact has suffered in the past and accounts for the history dependence of the contact law. $\delta_*$ is the (history dependent) overlap at which the force becomes zero when loading or unloading with the current (history dependent) stiffness $k_*$. $\delta_f$ is the overlap at which the force vanishes when the stiffness constant $k_2$ is used (at large overlaps).

limited by $-k_c\delta$, with the adhesion "stiffness" constant $k_c$.

### *2.2 Tangential Contact Force Laws*

In the tangential direction, the forces and torques depend on the tangential displacement and the relative rotations of the particle surfaces. Dynamic (sliding) and static *friction* depend on the tangential component of the relative velocity of the contact points,

$$\boldsymbol{v}_t = \boldsymbol{v}_{ij} - \boldsymbol{n}(\boldsymbol{n}\cdot\boldsymbol{v}_{ij}) \ , \text{ where } \quad \boldsymbol{v}_{ij} = \boldsymbol{v}_i - \boldsymbol{v}_j + a_i'\boldsymbol{n}\times\boldsymbol{\omega}_i + a_j'\boldsymbol{n}\times\boldsymbol{\omega}_j \quad (2)$$

is the relative velocity of the particle surfaces at contact. Here $a'_\alpha = a_\alpha - \delta/2$, for $\alpha = i, j$, is the corrected radius relative to the contact point. $\boldsymbol{v}_i$, $\boldsymbol{v}_j$, $\boldsymbol{\omega}_i$, and $\boldsymbol{\omega}_j$ are the linear and rotational velocities of particles $i$ and $j$, respectively.

Tangential forces $f^t$ acting on the contacts are modelled to be proportional to the accumulated sliding distance of the contact points along each other with a (tangential) stiffness constant $k_t$, i.e. $f^t = k_t \int v_t dt$, where $v_t$ is the

tangential component of the relative velocity of the contact point. Including also a viscous damping constant, $\gamma_t$, the tangential force is limited by the product of the normal force and the contact friction coefficient $\mu$, according to Coulombs law, $f^t \leq \mu f^n$. For more details see Ref. [25].

### *2.3 Background Friction*

Viscous dissipation as mentioned above takes place localized in a two-particle contact only. In the bulk material, where many particles are in contact with each other, this dissipation mode is very inefficient for long-wavelength cooperative modes of motion, especially when linear force laws are involved [55]. Therefore, an additional damping with the background is introduced, such that the total force $\boldsymbol{f}_i$ and torque $\boldsymbol{q}_i$ on particle $i$ are given by

$$\boldsymbol{f}_i = \sum_j \left( f^n \boldsymbol{n} + f^t \boldsymbol{t} \right) - \gamma_b \boldsymbol{v}_i \quad \text{and} \quad \boldsymbol{q}_i = \sum_j \boldsymbol{q}^{\text{friction}} - \gamma_{br} a_i^2 \boldsymbol{\omega}_i \ , \tag{3}$$

where the sums take into account all contact partners $j$ of particle $i$, and $\gamma_b$ and $\gamma_{br}$ are the (artificial) background damping viscosities assigned to the translational and rotational degrees of freedom, respectively. The viscosities can be seen as originating from a viscous inter-particle medium and enhance the damping in the spirit of a rapid relaxation and equilibration. Note that the effect of $\gamma_b$ and $\gamma_{br}$ should be checked for each set of parameters: it should be small in order to exclude artificial over-damping.

### *2.4 Contact model Parameters*

In the following we measure lengths in units of millimeters (mm), masses in milligrams (mg) and times in units of one hundred microseconds (100 $\mu$s). Note that only a few parameters have to be specified with dimensions, while the others are expressed as dimensionless ratios in Tab. 1.

A maximal stiffness constant of $k_2 = 5$, as used in our simulations, corresponds to a typical contact duration (half-period) $t_c \approx \sqrt{m/(2k)} \approx 6.5 \times 10^{-4}$, for a normal collision of a large and a small particle with $\gamma = 0$. Accordingly, an integration time-step of $t_{\text{MD}} = 5 \times 10^{-6}$ is used in order to allow for a "safe" integration of the equations of motion. Note that not only the normal "eigenfrequency" but also the eigenfrequencies for the rotational degrees of freedom have to be considered, as well as the viscous response times $t_\gamma \approx m/\gamma$. All of the (inverse) eigenfrequencies should be considerably larger than $t_{\text{MD}}$, while the viscous response times should be even larger, so that $t_\gamma > t_c \gg t_{\text{MD}}$.

| Property | Symbol | Value | dimensional units | SI-units |
|---|---|---|---|---|
| Time unit | $t_u$ | 1 | $100\,\mu$s | $10^{-4}$ s |
| Length unit | $x_u$ | 1 | 1 mm | $10^{-3}$ m |
| Mass unit | $m_u$ | 1 | 1 mg | $10^{-6}$ kg |
| Particle radius | $a_0$ | 0.005 | $5\,\mu$m | $5\,10^{-6}$m |
| Material density | $\rho$ | 2 | 2 mg/mm$^3$ | 2000 kg/m$^3$ |
| Max. loading/unloading stiffness | $k_2$ | 5 | $5$ mg/$(100\mu$s$)^2$ | $5\,10^2$ kg/s$^2$ |
| Initial loading stiffness | $k_1/k_2$ | 0.5 | | |
| Adhesion "stiffness" | $k_c/k_2$ | 0.2 | | |
| Friction stiffness | $k_t/k_2$ | 0.2 | | |
| Coulomb friction coefficient | $\mu = \mu_d = \mu_s$ | 1 | | |
| Dynamic to static friction ratio | $\phi_d = \mu_d/\mu_s$ | 1 | | |
| Normal viscosity | $\gamma = \gamma_n$ | $5 \times 10^{-5}$ | $5\,10^{-5}$ mg/$100\mu$s | $5\,10^{-7}$ kg/s |
| Tangential viscosity | $\gamma_t/\gamma$ | 0.2 | | |
| Background viscosity | $\gamma_b/\gamma$ | 4.0 | | |
| Background viscous torque | $\gamma_{br}/\gamma$ | 1.0 | | |
| Fluid overlap | $\phi_f$ | 0.05 | | |

Table 1
Microscopic material parameters used (third column), if not explicitly specified. The fourth column contains these values in the dimensional units, i.e., when the time-, length-, and mass-units are 100 $\mu$s, mm, and mg, respectively. Column five contains the parameters in SI-units. Energy, velocity, force, acceleration, and stress have to be scaled with factors of $10^{-4}$, $10^{-1}$, $10^{-1}$, $10^5$, and $10^5$, respectively, for a transition from reduced to SI-units.

A more detailed discussion of all the effects due to the interplay between the model parameters and the related times is, however, far from the scope of this paper. Details can be found in Ref. [25] and references therein.

## 3 Tablet preparation and material failure test

### *3.1 Tablet preparation*

Having introduced the model and its parameters in the last section here we describe the experimental idea and the steps of our simulations. We prepare a "tablet" (granule) consisting of primary particles that behave according to

the contact force laws mentioned above. A four-step process is applied:

- creation of a loose initial sample
- pressure sintering by isotropic compression
- removal of the pressure
- relaxation

On the resulting unconfined "tablet", or material sample, tests can be performed, e.g. controlled compression or tensile tests as well as sound wave propagation tests. Care has to be taken to perform first the preparation and later the tests in a symmetric way (see below) to avoid artefacts.

### *3.1.1 Initial sample*

Before sintering the first step is to *create a loose configuration* of $N = 1728$ spherical (granular) particles with a Gaussian distribution of radii with average $a = 0.005$. The tails of the distribution are cut off at 0.003 and 0.0075 to ensure that all particles are comparable in size [56], i.e. neither too large nor too small particles are desired. For the situations presented in this paper, the half-width of the distribution is $w_a = \sqrt{\langle a^2 \rangle - \langle a \rangle^2} = 0.0007213$. In addition, the initial velocities are drawn from a Gaussian distribution in each direction.

In the initial preparation stage the particles are arranged on a regular cubic lattice with wide spacing so that particles are not in contact – neither with each other nor with a wall – and have space to move and become disordered. Then the system is compressed with a pressure of $p_1 = 0.5$ to create a loose initial packing with a coordination number $\mathcal{C} = 5.89$ and volume fraction, $\nu = \sum_i V(a_i)/V = 0.607$, with the particle volume $V(a_i) = (4/3)\pi a_i^3$.

### *3.1.2 Pressure sintering*

The second step is *pressure sintering*: The system is compressed by keeping one wall in each spatial direction fixed while applying a constant pressure of $p_s = 10$ to the other (three) walls. During compression, the particles are frictional with a friction coefficient $\mu = 1$, and have zero adhesion amongst each other, i.e. $k_c = 0$. Four of the six walls are frictionless $\mu^{\text{wall}} = 0$ and cohesionless ($k_c = 0$). The remaining two (opposing) walls are already prepared for the tests to come. These two walls define the uni-axial direction and are strongly adhesive, with $k_c^{\text{wall}}/k_2 = 20$, so that the sample sticks to them, while all other walls can be easily removed in the third step. The wall-adhesion has no visble effect here, since the sample is strongly confined. In contrast, friction has an effect, i.e. friction with the walls would hinder the pressure to be transferred completely to its opposite wall. Frictional walls carry part of the load – an effect that is known since the early work of Janssen [57,58].

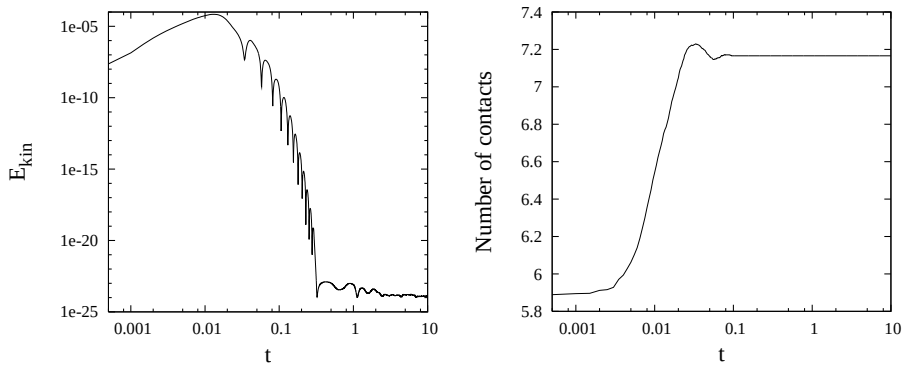


Fig. 2. Kinetic energy $E_{\mathrm{kin}}$ (left) and coordination number [number of contacts per particle] (right) as a function of time $t$ during isotropic pressure sintering with final pressure $p_s = 10$. Here the particle contacts are adhesionless, $k_c = 0$, while the other parameters are given in Tab. 1

During the compression the kinetic energy first increases and then decreases, see the left graph of Fig. 2, due to the energy dissipation in the system. We keep the pressure constant until the kinetic energy has very well reached a small constant value, within fluctuations, determined only by the numerical accuracy.

The right graph of Fig. 2 shows the mean coordination number as a function of time. The number of contacts increases during pressure sintering, overshoots, and finally settles to a constant value of $\mathcal{C} \approx 7.17$. Not surprisingly, a rather high volume fraction, $\nu = 0.6754$, is reached during the pressure sintering. (After stress-relaxation (see below), these values decrease considerably to $\nu \approx 0.626 \pm 0.005$ and $\mathcal{C} \approx 6.2 \pm 0.2$, depending on the material parameters used.

### *3.1.3 Pressure release*

Using this pressure sintered sample, the third step is to *remove the pressure* from the walls. Before we do so both $k_c$ and $\mu$ are set to the desired values ($k_c/k_2 = 0.2$ or 1.0 and $\mu = 1.0$, 0.1, or 0.0). The combination of material parameters and their identification codes are summarized in Tab. 2.

The control pressure is smoothly released from the walls in a co-sinusoidal way, starting from its sintering value, $p_s = 10$, down to a residual value, $p_0$, that is five orders of magnitude lower, i.e. $p_0/p_s = 10^{-5}$. The half period of the co-sinusoidal pressure release is $t_0 = 12.5$, but relaxation is continued further until the kinetic energy is dissipated and reaches tiny values, see Fig. 3. The small residual pressure keeps single particles from leaving the sample and also keeps the walls in place. This is important in order to not spoil the efficiency of our linked cell algorithm, where the cell size is a fraction of the system size between the walls. However, this confining stress $p_0$ is not big enough to affect the dynamics of the tests performed, it is just a convenient way to keep the

| Type | A | B | C | D | E | F |
|---|---|---|---|---|---|---|
| $k_c$ | 1 | 5 | 1 | 5 | 1 | 5 |
| $\mu$ | 1 | 1 | 0.1 | 0.1 | 0 | 0 |
| $\nu$ | 0.6270 | 0.6280 | 0.6296 | 0.6294 | 0.6273 | 0.6216 |
| $\mathcal{C}$ | 6.097 | 6.183 | 6.020 | 6.191 | 6.122 | 6.454 |

Table 2
Adhesion and friction parameters used during stress-release and for the further tests of the samples A-F. The densities and coordination numbers are realized after relaxation, after stress-release, before the subsequent compression and/or sound tests.

walls rather close to the sample. ($p_0/p_s = 10^{-3}$ leads to very similar results.)

There are qualitative differences for the short time behaviour between the samples A and B on the one hand and samples C – F on the other hand. In the latter samples the friction coefficient is suddenly reduced from $\mu = 1$ to smaller values just before the walls are removed. As an example, in Fig. 3 samples A and C are compared, which have $\mu = 1$, and 0.1, respectively. The kinetic energy of sample C increases instantaneously due to the "failure" of several contacts and subsequent dynamic reorganization. During this reorganization also the coordination number, see bottom panels in Fig. 3, increases slightly, as well as the density (data not shown). For sample E, the increase in kinetic energy, coordination number and density is larger, since the friction is reduced to an even smaller value $\mu = 0$ (data not shown).

A Comparison of samples B, D, and F leads to qualitatively similar observations as did the comparison of samples A, C, and E discussed above. The sudden reduction of friction has the same effect when $k_c = 5$ instead of $k_c = 1$. The increase in adhesion from $k_c = 1$ to $k_c = 5$ does not show a strong effect initially. Only for larger times, i.e. lower pressure, the effect of contact adhesion manifests itself in slightly shorter relaxation times. All densities are very similar, only the coordination number is systematically slightly larger for stronger adhesion.

### *3.1.4 Final relaxation*

The fourth preparation step is the *final relaxation* of the system. This is done in three substeps. First, immediately after the control pressure on the wall has reached its low residual value, the system is relaxed further until time $t_{r1} = 200$ with three fixed walls and three walls with the residual pressure reached at the end of the wall removal procedure. Second, after the kinetic energy has reached a small value, within fluctuations, for a long time, the system is further relaxed and symmetrized with the same pressure of $10^{-4}$ applied from *all* sides

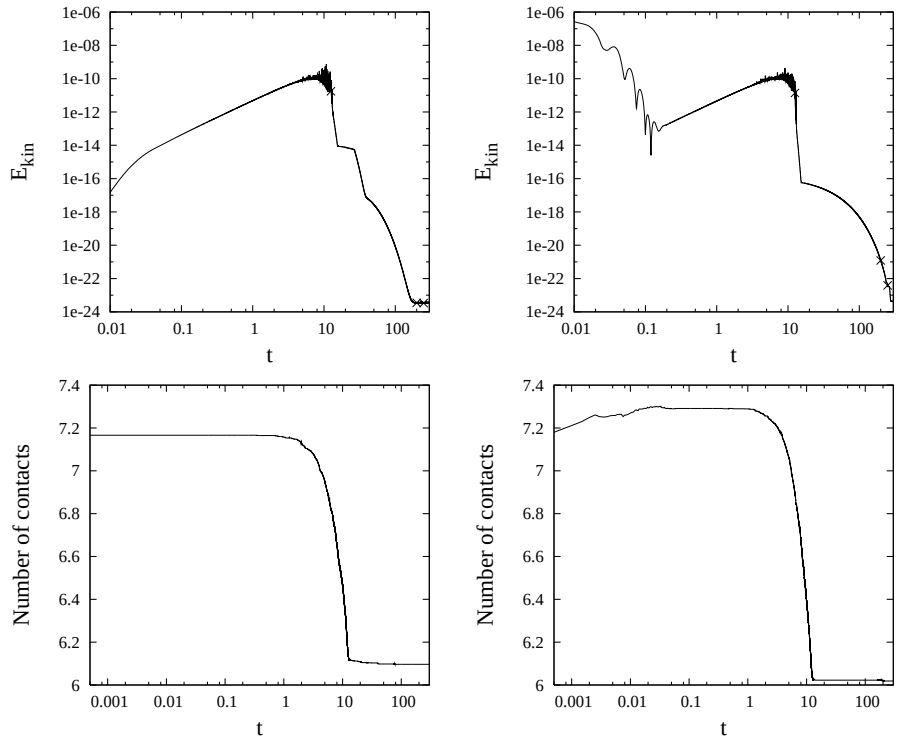


Fig. 3. Kinetic energy $E_{\mathrm{kin}}$ (top) and coordination number [number of contacts per particle] (bottom) as a function of time $t$ during stress-removal from the walls and subsequent relaxation. The material parameters are given in Tab. 1, for sample A (left), with $\mu = 1$, while the friction is reduced to $\mu = 0.1$ for sample C (right). The markers (top) show the the changes discussed in the text at times 12.5, 200, and 250.

for another time interval of $t_{r2} = 50$. In the final relaxation step, again a time interval of $t_{r3} = 50$, the two walls in the $x$-direction are fixed and the other four walls are kept at the residual pressure. We now have an unconfined sample with fixed walls in the $x$-direction and negligible stresses in all directions. The tests to be performed are uni-axially deforming the walls in the $x$ direction only.

The prepared sample can now be used for all sorts of further tests. In this paper we will show compression tests in the next subsection 3.2 and sound wave propagation on different samples in section 4, as sketched in Fig. 4.

### *3.2 Compression test*

In this section we describe an uni-axial unconfined compression test, starting from the final configuration of sample A from the previous subsection. This test resembles a direct measurement of the unconfined yield-strength, as applied in mechanical engineering and particle technology, see [59]. However, we apply

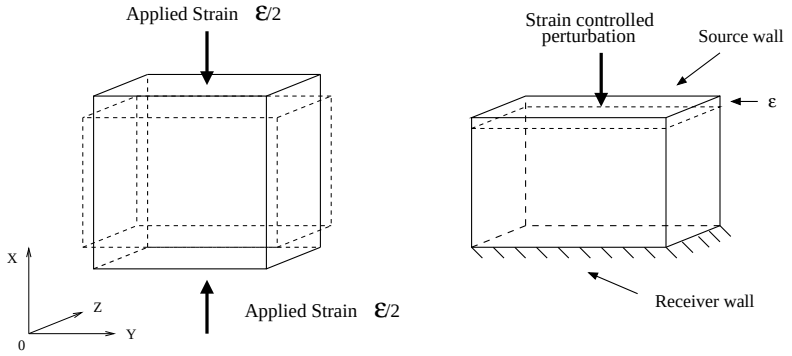


Fig. 4. Sketches of the compression (left) and the wave propagation (right) tests

the strain in several rather small steps. After each small step we relax the system in the compressed state, i.e. we run the simulation for a while without changing the pressure ($y$- and $z$-directions) on and positions ($x$-direction) of the walls. We later perform tests on these "relaxed" states. This must not be confused with a test performed after the stress has been removed.

Instead of applying the target-strain of $\epsilon_{max} = 0.0217$ in one sweep, the deformation is divided into 10 steps, with $\epsilon_s \approx 0.00217$ each (measured relative to the initial system size). This leads to states with $\epsilon_m = m\epsilon_s$, with integer $m = 0, 1, 2, ..., 10$. During each of the ten strain-steps, the system is compressed in a co-sinusoidal way for one half-period, during a time interval of $t_\epsilon = 0.5$, and then relaxed for a time interval of $t_{\epsilon r} = 4.5$. Note that the results are rate dependent (where the rate is proportional to $1/t_\epsilon$). A low enough rate has to be chosen in order to stay in the quasi-static regime. Fig. 5 gives a comparison with a ten times higher rate (left graph). A four times higher rate does not change qualitatively the stress-strain behaviour (data not shown here). The "relaxed" sample (which is still under anisotropic pressure) is then further deformed and relaxed and this is repeated again and again. The reason for this intermediate relaxation is that we want to perform sound wave propagation tests on well-defined "relaxed", static samples after those have suffered from different levels of deformation,

The stress-strain diagram of this compression test is shown in Fig. 5. The initial stress-strain relation is very close to linear, with a slope of $D = \partial\sigma/\partial\epsilon = 225.6$. The maximal stress in is approximately 1/4 of the previously applied sintering pressure $p_s$. Additionally, we see that relaxing the system in the elastic regime, at intermediate strains of $\epsilon_{1-4}$, leads to samples very close to the elastic branch. Thus up to a strain of about one percent the system behaves almost like an elastic solid. Tab. 3 summarizes the strains, coordination numbers, and volume fractions for all $\epsilon_m$ investigated.

At larger deformation, $\epsilon_5$, the sample starts to fail: Here the stress is close to its maximum and during the relaxation the stress decreases, i.e. we have left

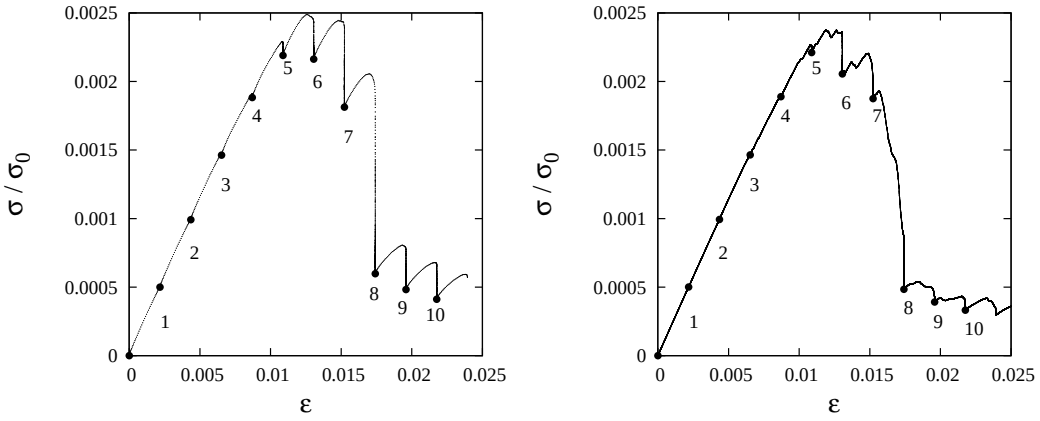


Fig. 5. Normalized axial stress $\sigma/\sigma_0$ plotted against the axial strain $\epsilon$ from a step–wise uni-axial compression test. The reference stress, $\sigma_0 = k_2/a$, is used to non-dimensionalize the stress. The left graph shows the results for a rate ten times faster than the one used in the following (right graph). The points indicate the configurations on which sound propagation tests are performed in Sec. 4.

| Type | $\epsilon_0$ | $\epsilon_1$ | $\epsilon_2$ | $\epsilon_3$ | $\epsilon_4$ | $\epsilon_5$ | $\epsilon_6$ | $\epsilon_7$ | $\epsilon_8$ | $\epsilon_9$ | $\epsilon_{10}$ |
|---|---|---|---|---|---|---|---|---|---|---|---|
| $\epsilon$ in % | 0% | 0.22% | 0.43% | 0.65% | 0.87% | 1.09% | 1.30% | 1.52% | 1.74% | 1.95% | 2.17% |
| $C$ | 6.097 | 6.098 | 6.093 | 6.090 | 6.086 | 6.001 | 5.810 | 5.592 | 4.679 | 4.612 | 4.556 |
| $\nu$ | 0.627 | 0.627 | 0.627 | 0.624 | 0.620 | 0.613 | 0.594 | 0.578 | 0.546 | 0.537 | 0.526 |

Table 3
Strain steps $\epsilon_m$ and corresponding coordination numbers and volume fractions. The round-off error for the given values is $\pm 10^{-3}$

the elastic regime. The coordination number and density decrease considerably when the sample starts to fail. At the next strain levels, $\epsilon_6$, and $\epsilon_7$, the stress remains large but the stress decreases more and more during relaxation. At $\epsilon_8 \approx 0.017$ the system fails and becomes almost fluid-like with an enormous decay of stress during relaxation. Also for later compression steps the stress is significantly reduced, relative to the maximum, during the relaxation process, though it never reaches zero.

## 4 Sound wave propagation tests

The goal of this section is to characterize how the propagation of sound waves is influenced by, on the one hand, the "microscopic" parameters such as the inter-particle cohesion and friction and, on the other hand, the material state (uncompressed, uni-axially compressed in the elastic regime, close to failure, or in the fluidized softening regime). This is done by analyzing the wave propagation, phase velocities, damping, and Fourier spectra of the sound waves propagating through the system.

The "microscopic" inter-particle interaction laws (material properties) have an influence on the propagation of sound. Therefore we first probe packings with different "microscopic" adhesion and friction parameters. When a tablet undergoes strain, both microscopic (contact scale) and macroscopic (multi-grain scale) changes occur in the structure. In order to investigate the change of the macroscopic material properties due to these reorganisations we probe the packing at various externally applied uni-axial strains, corresponding to the different regimes mentioned above. Note that a piecewise linear contact law with history-dependent stiffness (see Sec. 2) allows to decouple the non-linearity of the contact forces (as in the case of the Hertz contact model for example) from the influence of reorganisations and opening or closing of contacts.

For the sound propagation tests we start with the tablets prepared as described in Sec. 3. The tablet has two fixed walls in the $x-$ direction and virtually free boundary conditions in the other two directions. Now a signal is sent through the sample by applying a time-dependent variation of the position (according to the desired signal) to one of the two walls, see left sketch of Fig. 4. After some time the opposite wall will feel a stress variation which we analyze and interpret, right sketch of Fig. 4. The wave form is a full period of a co-sine, moving the wall in and out, with an amplitude, $A = 10^{-7}$ and a time period $T = 3.\,10^{-3}$. This stress amplitude is much smaller than the maximum stress in Fig. 5.

### *4.1 Influence of cohesion and friction on sound propagation*

In this subsection the influence of the microscopic parameters adhesion and friction on the sound propagation of an uncompressed tablet is studied. In Tab. 2 the values used for inter-particle adhesion $k_c$ and friction $\mu$ are given along with the sample names A, B, C, D, E, or F. In Fig. 6, the source (left) and receiver (right) signals (stress at the wall) are plotted versus time. Tab. 4 gives the wave velocities, calculated for different reference points as specified below, and the damping ratios between the source and receiver signals.

Wave velocities are deduced from the time of flight (TOF). Therefore a reference point is chosen at the maximum of the peak (leading to the velocity $v_m$), at 5% of that maximum ($v_5$), at 10% of that maximum ($v_{10}$) or finally when the signal reaches for the first time zero amplitude after the peak ($v_0$). The ratio of the distance between the two walls (source and receiver) and the time difference between the two signals gives the desired wave velocities. Note that since the medium is dispersive, the calculated velocities are an approximation of the group velocity for the range of propagating frequencies.

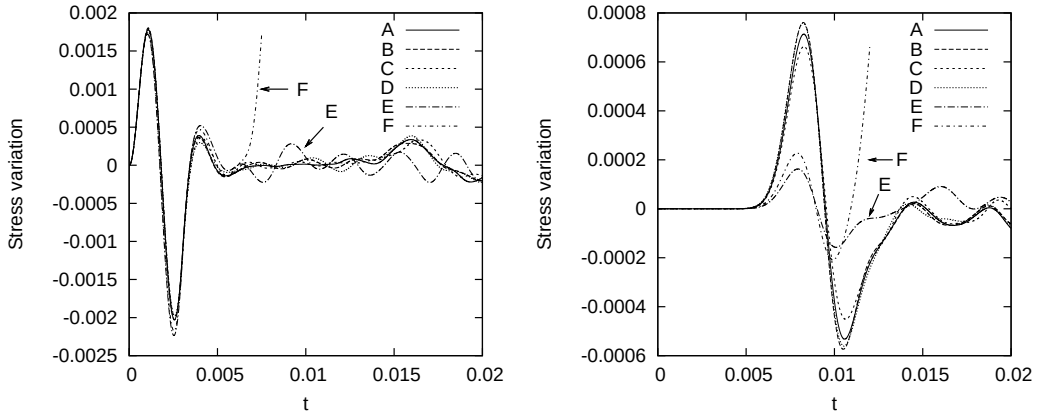


Fig. 6. Stress variation $\sigma(t) - \sigma(0)$ as function of time $t$ at the source and receiver walls for the samples prepared in Sec. 3.1. Here $\sigma(0)$ denotes the pressure at the wall just before the sound propagation test started. Note the different vertical axes. The signal for sample F has been cut off as it oscillates strongly later on.

| Type | A | B | C | D | E | F |
|---|---|---|---|---|---|---|
| $v_5$ | 19.6 | 19.63 | 19.6 | 19.69 | 20.23 | 20.24 |
| $v_{10}$ | 18.89 | 18.94 | 18.91 | 18.99 | 19.52 | 19.55 |
| $v_m$ | 15.99 | 16.05 | 15.95 | 16.07 | 16.62 | 16.7 |
| $v_0$ | 14.94 | 15.04 | 14.84 | 15.03 | 15.71 | 15.86 |
| $\sigma_d$ | 2.49 | 2.37 | 2.65 | 2.35 | 10.59 | 7.67 |

Table 4
Velocities, $v$, as defined in the main text and damping $\sigma_d$.

The damping ratios $\sigma_d$ are calculated by dividing the maximum of the peak of the source signal by the corresponding peak of the receiver signal. Those ratios depend on the distance between the two walls and on the dispersion.

The results show a clear difference between the specimens with friction (A, B, C, and D) and the frictionless cases (E and F) concerning both damping and velocities. The damping (as defined above) is significantly stronger for cases E and F. This may be due to the fact that friction strengthens the specimen and hence enhances the wave transmission, i.e. reduces damping in accordance with previous results [28]. The strong reduction in the peak amplitude of the frictionless samples might also be related to the different configuration structure of the samples. For the frictional specimens (A – D) the damping is lower for higher adhesion (B and D). The same is observed for frictionless specimens, which means that stronger adhesion enhances the wave transmission as well.

Concerning the velocities, for the same inter-particle adhesion, A, C & E and B, D & F, all velocities are systematically lower in the frictional cases (A

– D) than in the frictionless samples (E and F). In a previous study [28] the velocity of sound was higher in the frictional case, where identical samples were prepared without friction before activating the desired friction coefficient. This is in contrast to our results, where all samples are different. However, a complex interplay between frictional and cohesional effects might be the explanation for this unexpected result. Finally, when comparing specimens A and C with specimens B and D, there is a slight increase of velocities with higher cohesion. The same is observed when comparing specimens E and F. This suggests again that adhesion increases the effective stiffness of the material and thus the wave speed. The fact that adhesion increases the tensile strength was examined and reported in [25,26]. Note that the increase of velocity is correlated with the increase of coordination number for increasing contact adhesion and thus depends on the history of the sample.

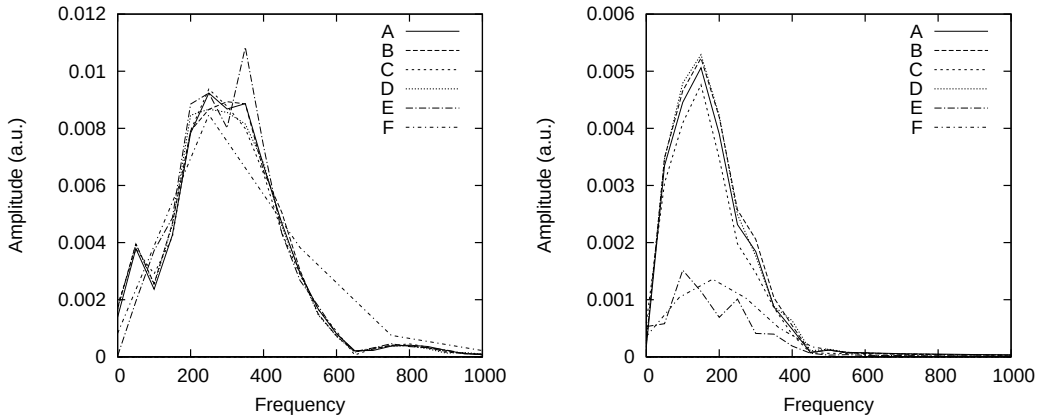


Fig. 7. Power spectrum from (left) source- and (right) receiver-signals, taken from the simulations in Fig. 6 in arbitrary units (a.u.). Only signals E and F behave differently from the others, reflecting their higher damping rates (see right graph).

From the power spectra, obtained by applying the Fourier transform to the time signals, the dispersive and filtering behaviour of the system can be identified by the observed significant shift of the main frequency from about 330 down to 150 (corresponding to 33 kHz and 15 kHz in SI-units), see Fig. 7. The granular, and hence inhomogeneous and discrete, nature of the system leads to its dispersive behaviour. High frequencies are very sensitive to the details at the grain scale because their wavelengths are small, and hence they travel more slowly and less far than lower frequencies. The latter ones are less sensitive to the details at the grain scale because their wavelengths are much larger and average over many grains. Note that the main frequency at around 330 comes from the chosen period for the wave form, $T = 3.\,10^{-3}$, see the beginning of Sec. 4. Besides the evidently strong damping of signals E and F, no further striking differences are observed for the different specimens' spectra. Even though there are differences in the power law tail of the spectra (data not shown), we could not correlate those to the different parameters.

In the following, the compressed specimen A (uni-axially, from both sides) is used. In that special direction the wall movement is strain controlled and the other two directions are virtually free boundaries, see Sec. 3.2 for details. At each step of the compression test, after relaxation, see Fig. 5, a sound wave is sent through the system the same way as in the previous subsection. Fig. 8 shows the signals at the source and receiver walls.

Regarding $v_m$ and $v_0$, see Tab. 5, the velocities seem to increase a little as the system is further compressed until state $\epsilon_3$. Then they slightly decrease until state $\epsilon_6$ and finally the decay is stronger until the last state $\epsilon_{10}$. This variation correlates with the three regimes observed on the stress-strain curve, see Fig. 5, i.e. first the close-to-linear regime, second, the start-of-failure regime, and finally the critical-flow regime. The damping strongly increases for the last steps, $\epsilon_8$ to $\epsilon_{10}$, as the sample is not really a solid any more. These observations correlate with the given coordination numbers $C$ and the density $\nu$, see Tab. 3. Similar observations are made concerning the power spectra of those signals, see Fig. 9, noting a stronger damping at steps $\epsilon_8$ to $\epsilon_{10}$. Additional studies are needed to determine whether the sound pulse method could allow for a sensitive material state characterization at all.

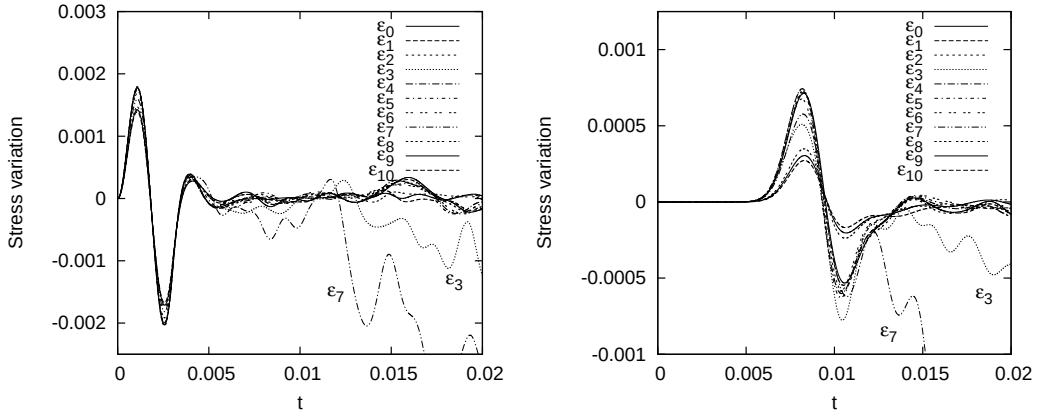


Fig. 8. Stress variation $\sigma(t) - \sigma(0)$ as function of time $t$ at the source and receiver walls, where the $\epsilon_3$ and $\epsilon_7$ signals display a different coda. Note the different vertical axes.

## 5 Conclusions

We have performed particle simulations of sound propagation in isotropically pressure sintered powder samples at very small confining stress. Using a recently proposed piecewise linear contact model for particle-particle interactions we probed different values of friction and adhesion during preparation.

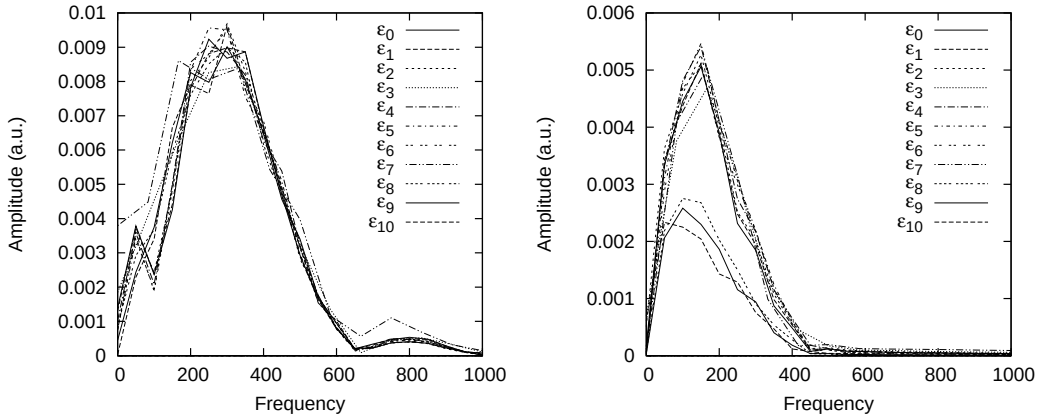


Fig. 9. Power spectra from source- and receiver-signals, taken from the simulations in Fig. 8 in arbitrary units (a.u.).

| Type | $\epsilon_0$ | $\epsilon_1$ | $\epsilon_2$ | $\epsilon_3$ | $\epsilon_4$ | $\epsilon_5$ | $\epsilon_6$ | $\epsilon_7$ | $\epsilon_8$ | $\epsilon_9$ | $\epsilon_{10}$ |
|---|---|---|---|---|---|---|---|---|---|---|---|
| $v_5$ | 19.6 | 19.59 | 19.6 | 20.00 | 19.58 | 19.56 | 19.55 | 19.45 | 19.26 | 19.24 | 19.14 |
| $v_{10}$ | 18.89 | 18.89 | 18.89 | 19.31 | 18.88 | 18.87 | 18.85 | 18.74 | 18.55 | 18.52 | 18.45 |
| $v_m$ | 15.99 | 16.01 | 16.03 | 16.13 | 16.05 | 16.06 | 16.04 | 15.84 | 15.66 | 15.58 | 15.54 |
| $v_0$ | 14.94 | 14.99 | 15.05 | 15.22 | 15.10 | 15.14 | 15.14 | 14.81 | 14.56 | 14.46 | 14.39 |
| $\sigma_d$ | 2.49 | 2.47 | 2.47 | 3.47 | 2.37 | 2.37 | 2.45 | 2.76 | 4.21 | 4.68 | 5.11 |

Table 5
Velocities, $v$, as defined in the main text and damping $\sigma_d$

In particular, we applied a P-wave on one end of the sample and measured and analyzed the signal on the opposing receiver wall. Surprisingly we found only very weak differences except for the frictionless case, where the velocity of sound was higher and the damping was stronger. Even though the samples were prepared using the same preparation protocol they evolved to different initial configurations due to different values of the contact parameters. The material behaviour is history dependent but mostly determined by the sintering pressure $p_s$ rather than by those paterial parameters varied here.

In addition, one of the samples was subjected to strain-controlled uni-axial unconfined compression and the sound propagation properties were studied at various levels of strain: In the elastic regime, at the onset of and during failure, and in the softening and flowing regimes. Even though in the elastic regime we found astonishingly little variation in the wave propagation velocity as a function of the strain, one particular sample behaved qualitatively different. In the softening regime all samples were unstable even though the amplitude of the probing pulse was 100 times smaller than the typical particle-particle overlap.

Having observed rather small differences between the different uni-axial strain

states, the expected dependence of sound propagation on the uni-axial anisotropic stress states studies was not observed.

The quantitative tuning of the DEM model to real experimental data remains a challenge for future research. The results presented here have units that are not supposed to mimic a real material. Some tuning can be done by rescaling, but a real fine-adjustment will require a more systematic study of other contact model parameters.

## Acknowledgements

Valuable discussions with J. Tomas, A. Suiker, L. Brendel, and W. Mulder are appreciated. This study was supported by the Delft Centre for Materials Self-Healing program, the research institute IMPACT of the University of Twente, and the Stichting voor Fundamenteel Onderzoek der Materie (FOM), financially supported by the Nederlandse Organisatie voor Wetenschappelijk Onderzoek (NWO), through the FOM-SHELL program and the Granular Matter program.

## References

[1] H. M. Jaeger, C. Liu, S. R. Nagel, Relaxation at the angle of repose, Phys. Rev. Lett. 62 (1) (1989) 40–43.

[2] H. M. Jaeger, C. Liu, S. R. Nagel, T. A. Witten, Friction in granular flows, Europhys.Lett. 11 (7) (1990) 619–624.

[3] H. M. Jaeger, S. R. Nagel, Physics of the granular state, Science 255 (1992) 1523.

[4] R. P. Behringer, The dynamics of flowing sand, Nonlinear Science Today 3 (1993) 1–15.

[5] H. J. Herrmann, J.-P. Hovi, S. Luding (Eds.), Physics of dry granular media - NATO ASI Series E 350, Kluwer Academic Publishers, Dordrecht, 1998.

[6] I. Goldhirsch, G. Zanetti, Clustering instability in dissipative gases, Phys. Rev. Lett. 70 (11) (1993) 1619–1622.

[7] R. P. Behringer, G. W. Baxter, Pattern formation and complexity in granular flow, in: A. Mehta (Ed.), Granular Matter, 1994, p. 85.

[8] S. Luding, E. Clément, A. Blumen, J. Rajchenbach, J. Duran, Studies of columns of beads under external vibrations, Phys. Rev. E 49 (2) (1994) 1634.

[9] N. Sela, I. Goldhirsch, Hydrodynamic equations for rapid flows of smooth inelastic spheres to Burnett order, J. Fluid Mech. 361 (1998) 41–74.

[10] O. Herbst, M. Huthmann, A. Zippelius, Dynamics of inelastically colliding spheres with Coulomb friction: Relaxation of translational and rotational energy, Granular Matter 2 (4) (2000) 211–219.

[11] O. Herbst, R. Cafiero, A. Zippelius, H. J. Herrmann, S. Luding, A driven two-dimensional granular gas with Coulomb friction, Phys. Fluids 17 (2005) 107102.

[12] A. Santos, Does the chapmanenskog expansion for sheared granular gases converge?, Phys. Rev. Lett. 100 (2008) 078003.

[13] J. Tomas, Fundamentals of cohesive powder consolidation and flow, Granular Matter 6 (2/3) (2004) 75–86.

[14] A. Castellanos, The relationship between attractive interparticle forces and bulk behavior in dry and uncharged fine powders, Advances in Physics 54 (4) (2005) 263–376.

[15] S. Luding, Shear flow modeling of cohesive and frictional fine powder, Powder Technology 158 (2005) 45–50.

[16] S. Luding, Anisotropy in cohesive, frictional granular media, J. Phys.: Condens. Matter 17 (2005) S2623–S2640.

[17] V. Richefeu, F. Radjai, M. S. El Youssoufi, Stress transmission in wet granular materials, Eur. Phys. J. E 21 (4) (2006), pp. 359-369.

[18] C. Thornton, K. K. Yin, Impact of elastic spheres with and without adhesion, Powder Technol. 65 (1991) 153.

[19] C. Thornton, K. K. Yin, M. J. Adams, Numerical simulation of the impact fracture and fragmentation of agglomerates, J. Phys. D: Appl. Phys. 29 (1996) 424–435.

[20] K. D. Kafui, C. Thornton, Numerical simulations of impact breakage of spherical crystalline agglomerate, Powder Technology 109 (2000) 113–132.

[21] C. Thornton, S. J. Antony, Quasi-static deformation of a soft particle system, Powder Technology 109 (1-3) (2000) 179–191.

[22] S. Luding, K. Manetsberger, J. Muellers, A discrete model for long time sintering, Journal of the Mechanics and Physics of Solids 53(2) (2005) 455–491.

[23] S. Luding, About contact force-laws for cohesive frictional materials in 2d and 3d, in: P. Walzel, S. Linz, C. Krülle, R. Grochowski (Eds.), Behavior of Granular Media, Shaker Verlag, 2006, pp. 137–147, band 9, Schriftenreihe Mechanische Verfahrenstechnik, ISBN 3-8322-5524-9.

[24] S. Luding, Contact models for very loose granular materials, in: P. Eberhard (Ed.), Symposium on Multiscale Problems in Multibody System Contacts, IUTAM Bookseries Vol. 1, Springer, Dordrecht, The Netherlands, 2007, pp. 135–150.

[25] S. Luding, Cohesive frictional powders: Contact models for tension, Granular Matter 10(4) (2008) 235–246.

[26] S. Luding, A. Suiker, Self-healing of damaged particulate materials through sintering, submitted (2008).

[27] O. Mouraille, S. Luding, Sound propagation in dense, frictional granular materials., in: R. Garcia-Rojo, H. J. Herrmann, S. McNamara (Eds.), Powders and Grains 2005, A. A. Balkema, Leiden, 2005, p. 319.

[28] O. Mouraille, W. A. Mulder, S. Luding, Sound wave acceleration in granular materials, J. Stat. Mech. (2006) P07023.

[29] S. Luding, Granular media: Information propagation, Nature 435 (2005) 159–160.

[30] O. Mouraille, S. Luding, Mechanic waves in sand: Effect of polydispersity, in: W. Peukert (Ed.), Partec 2007, 2007, CD proceeding.

[31] O. Mouraille, S. Luding, Sound wave propagation in weakly polydisperse granular materials, in press (2008).

[32] X. Jia, Codalike multiple scattering of elastic waves in dense granular media., Phys. Rev. Lett. 93(15) (2004) 154303.

[33] X. Jia, C. Caroli, B. Velicky, Ultrasound propagation in externally stressed granular media., Phys. Rev. Lett. 82(9) (1999) 1863.

[34] S. R. Hostler, C. E. Brennen, Pressure wave propagation in a shaken granular bed, Phys. Rev. E 72 (2005) 031304.

[35] P. A. Cundall, O. D. L. Strack, A discrete numerical model for granular assemblies, Géotechnique 29 (1) (1979) 47–65.

[36] Y. M. Bashir, J. D. Goddard, A novel simulation method for the quasi-static mechanics of granular assemblages, J. Rheol. 35 (5) (1991) 849–885.

[37] C. Thornton, Numerical simulations of deviatoric shear deformation of granular media, Géotechnique 50 (1) (2000) 43–53.

[38] C. Thornton, L. Zhang, A DEM comparison of different shear testing devices, in: Y. Kishino (Ed.), Powders & Grains 2001, Balkema, Rotterdam, 2001, pp. 183–190.

[39] P. A. Vermeer, S. Diebels, W. Ehlers, H. J. Herrmann, S. Luding, E. Ramm (Eds.), Continuous and Discontinuous Modelling of Cohesive Frictional Materials, Springer, Berlin, 2001, Lecture Notes in Physics 568.

[40] M. H. Sadd, G. Adhikari, F. Cardoso, DEM simulation of wave propagation in granular materials., Powder Technology 109(1-3) (2000) 222–233.

[41] C. Liu, S. R. Nagel, Sound in sand, Phys. Rev. Lett. 68 (15) (1992) 2301–2304.

[42] C. S. Chang, S. J. Chao, Y. Chang, Estimates of elastic moduli for granular material with anisotropic random packing structure, Int. J. Solids & Structures 32 (14) (1995) 1989–2009.

[43] A. Shlivinski, K. J. Langenberg, Defect imaging with elastic waves in inhomogeneous-anisotropic materials with composite geometries, Ultrasonics 46(1) (2007) 89–104.

[44] Q. M. Tai, M. H. Sadd, A discrete element study of the relationship of fabric to wave propagational behaviours in granular materials., Int. J. for Num. and Analytic Meth. in Geomechanics 21(5) (1997) 295–311.

[45] V. Tournat, B. Castagnede, V. Gusev, P. Bequin, Self-demodulation acoustic signatures for nonlinear propagation in glass beads., Comptes Rendus Mecaniques 331(2) (2003) 119–125.

[46] V. F. Nesterenko, Dynamics of Heterogeneous Materials, Springer-Verlag New York, 2001.

[47] N. Dejong, L. Hoff, T. Skotland, N. Bom, Absorption and scatter of encapsulated gas filled microspheres - theoretical considerations and some measurements, Ultrasonics 30(2) (1992) 95–103.

[48] P. A. Vermeer, W. Ehlers, H. J. Herrmann, E. Ramm (Eds.) Modelling of Cohesive-Frictional Materials, Balkema at. Taylor & Francis, Leiden, Netherlands 2004, (ISBN 04 1536 023 4).

[49] I. Agnolin, J. T. Jenkins, L. L. Ragione, A continuum theory for a random array of identical, elastic, frictional disks, Mechanics of Materials 38(8-10) (2006) 687–701.

[50] V. Tournat, private communication (2007).

[51] M. Lätzel, S. Luding, H. J. Herrmann, D. W. Howell, R. P. Behringer, Comparing simulation and experiment of a 2d granular Couette shear device, Eur. Phys. J. E 11 (4) (2003) 325–333.

[52] M. P. Allen, D. J. Tildesley, Computer Simulation of Liquids, Oxford University Press, Oxford, 1987.

[53] D. C. Rapaport, The Art of Molecular Dynamics Simulation, Cambridge University Press, Cambridge, 1995.

[54] T. Pöschel, T. Schwager, Computational Granular Dynamics, Springer, Berlin, 2005.

[55] S. Luding, E. Clément, A. Blumen, J. Rajchenbach, J. Duran, Anomalous energy dissipation in molecular dynamics simulations of grains: The "detachment effect", Phys. Rev. E 50 (1994) 4113.

[56] C. T. David, R. G. Rojo, H. J. Herrmann, S. Luding, Hysteresis and creep in powders and grains, in: R. Garcia-Rojo, H. J. Herrmann, S. McNamara (Eds.), Powders and Grains 2005, Balkema, Leiden, Netherlands, 2005, pp. 291–294.

[57] H. A. Janssen, Versuche über Getreidedruck in Silozellen, Zeitschr. d. Vereines deutscher Ingenieure 39 (35) (1895) 1045–1049.

[58] M. Sperl, Experiments on corn pressure in silo cells. translation and comment of Janssen's paper from 1895, Granular Matter 8 (2) (2006) 59–65.

[59] J. Schwedes, Review on testers for measuring flow properties of bulk solids, Granular Matter 5 (1) (2003) 1–45.